

DIMENSION: Dynamic MR Imaging with Both K-space and Spatial Prior Knowledge Obtained via Multi-Supervised Network Training

Shanshan Wang, *Member, IEEE*, Ziwen Ke, Huitao Cheng, Sen Jia, Ying Leslie, Hairong Zheng and Dong Liang, *Senior Member, IEEE*

Abstract—Dynamic MR image reconstruction from incomplete k-space data has generated great research interest due to its capability in reducing scan time. Nevertheless, the reconstruction problem is still challenging due to its ill-posed nature. Most existing methods either suffered from long iterative reconstruction time or explored limited prior knowledge. This paper proposes a dynamic MR imaging method with both k-space and spatial prior knowledge integrated via multi-supervised network training, dubbed as DIMENSION. Specifically, DIMENSION consists of a Fourier prior network for k-space completion and a spatial prior network for capturing image structures and details. Furthermore, a multi-supervised network training technique is developed to constrain the frequency domain information and reconstruction results at different levels. The comparisons with k-t FOCUSS, k-t SLR, L+S and the state-of-the-art CNN method on in vivo datasets show our method can achieve improved reconstruction results in shorter time.

Index Terms—Dynamic MR imaging, deep learning, compressed sensing, k-space prior, multi-supervised

I. INTRODUCTION

DYNAMIC MR imaging is a non-invasive imaging technique which could provide both spatial and temporal information for the underlying anatomy. Nevertheless, both physiological and hardware constraints have made it suffer from slow imaging speed or long imaging time, which may lead to patients discomfort or sometimes cause severe motion artifacts. Therefore, it is of great necessity to accelerate MR imaging.

To accelerate dynamic MR scan, there have been three main directions of efforts, namely in developing physics based fast imaging sequences [1], hardware based parallel imaging techniques [2] and signal processing based MR image reconstruction methods from incomplete k-space data. Our specific focus here is the undersampled MR image reconstruction, which

requires prior information to solve the aliasing artifacts caused by the violation of the Nyquist sampling theorem. Specifically, the reconstruction task is normally formulated as solving an optimization problem with two terms i.e. data fidelity and prior regularization. Popular prior information includes sparsity, which prompts image to be sparsely represented in a certain transform domain while being reconstructed from incoherently undersampled k-space data. These techniques are well-known as compressed sensing MRI (CS-MRI) [3–5]. For example, k-t BLAST and k-t SENSE [6] take advantage of a priori information about the x-f support obtained from the training data set in order to enhance the image resolution during data acquisition time. Using a random k-t sampling pattern and FOCUSS algorithm, k-t FOCUSS [7] is asymptotically optimal from the compressed sensing theory and encompasses the celebrated k-t BLAST and k-t SENSE as special cases. And k-t SLR [8] exploits the correlations in the dynamic imaging dataset by modeling the data to have a compact representation in the Karhunen Louve transform (KLT) domain. Low-rank matrix methods as derivatives of compressed sensing, enable one to complete missing or corrupted entries of a matrix through low-rank and incoherence conditions. Methods based on low-rank matrix completion [9] construct a space-time matrix where its each column corresponds to a temporal frame for dynamic MRI. Dictionary learning (DL) has also been investigated. DLTG [10] bases on a sparsity model that can learn redundancy in the data and an auxiliary constraint on TG sparsity. These methods have made great progresses in dynamic imaging and achieved improved results. Nevertheless, these methods only draw prior knowledge from limited samples. Furthermore, the reconstruction is iterative and sometimes time-consuming.

On the other hand, deep learning has shown great potential in accelerating MR imaging. There have been quite a few newly proposed methods, which can be roughly categorized into two types, model-based unrolling methods [11–13] and end-to-end learning methods [14–22]. The model based unrolling methods are to formulate the iterative procedure of traditional optimization algorithm to network learning. They adaptively learn all the parameters of regularization term and transforms in the model by network training. For example, ADMM-Net [11] is defined over a data flow graph, which is derived from the iterative procedures in Alternating Direction Method of Multipliers (ADMM) algorithm for optimizing a CS-based MRI model. In VN-Net [12], generalized com-

This research was partly supported by the National Natural Science Foundation of China (61601450, 61471350), the Natural Science Foundation of Guangdong (2015A020214019 and 2015A030310314), the Basic Research Program of Shenzhen (JCYJ20160531183834938, JCYJ20150831154213680, and JCYJ20140610151856736), and Key Laboratory for Magnetic Resonance and Multimodality Imaging of Guangdong Province (2014B030301013). DIMENSI author.

Shanshan Wang, Ziwen Ke contributed equally to this manuscript

S. Wang, Z. Ke, H. Cheng, S. Jia, H. Zheng and D. Liang are with Paul C. Lauterbur Research Center for Biomedical Imaging, Shenzhen Institutes of Advanced Technology, Chinese Academy of Sciences, Shenzhen 518055, China (e-mail: sophiasswang@hotmail.com; dong.liang@siat.ac.cn).

L. Ying is with the Department of Biomedical Engineering and the Department of Electrical Engineering, University at Buffalo, The State University of New York, Buffalo, NY 14260 USA

pressed sensing reconstruction formulated as a variational model is embedded in an unrolled gradient descent scheme. The other type utilizes the big data information to learn a network that map between the undersampled and fully sampled data pairs. Wang et al. [14] trained a deep neural network to learn the mapping relationship between undersampled brain MR images and fully sampled brain MR images. This is the first time to integrate deep architectures into fast MRI. AUTOMAP [17] has been proposed that learns a mapping between the sensor and the image domain to emerge from an appropriate corpus of training data. Despite all the successes, there are only two works that specifically apply to dynamic MR imaging [21, 22]. Both of these two works use a cascade of neural networks to learn the mapping between undersampling and full sampling cardiac MR images. Both works made great contributions to dynamic MR imaging. Nevertheless, the reconstruction results can still be improved since they consider all levels of features equally with only one supervised loss function and they just learn in image domain without combining frequency domain information sufficiently.

In this work, we propose a **DynamIc MR** imaging method with both **k-space** and **Spatial** prior knowledge integrated via **multi-supervised netwOrk traiNing**, dubbed as **DIMENSION**. The improvement is mainly reflected in two aspects: firstly, in the terms of network structure, we introduce the frequency domain learning into the network, so that the entire network can learn both frequency domain and spatial domain information at the same time; secondly, in terms of loss function, we propose multi-supervised loss function strategy, which can constrain the frequency domain information and reconstruction results at different levels. Our contributions could be summarized as follows:

- 1) In the present study, a novel dynamic MR imaging method with both k-space and spatial prior knowledge integrated via multi-supervised network training is proposed, which can combine the frequency domain and spatial domain information sufficiently. This is the first time to introduce cross-domain learning into MR cardiac imaging.
- 2) We propose a multi-supervised loss function strategy, which can constrain the frequency domain information and reconstruction results at different levels. Such loss strategy can guarantee that the frequency domain learning gets better completed k-space, and can make the reconstruction results of different levels in the spatial domain learning closer to the full sampling MR images. Here, we regard a loss function as a supervision.
- 3) Experimental results show that the proposed method is superior to conventional CS-based methods such as k-t FOCUSS and k-t SLR, as well as the state-of-the-art CNN-based method, DC-CNN. This fully demonstrates the effectiveness of progressive loss and cross-domain learning in cardiac MR imaging.

II. METHODOLOGY

A. CS-MRI and CNN-MRI

According to compressed sensing (CS) [3–5], MR images with a sparse representation in some transform domain can be

reconstructed from randomly undersampled k-space data. Let $\mathbf{x} \in \mathbb{C}^{N_x N_y N_t}$ represent a complex-valued dynamic MR image. Our problem can be described by the following formula:

$$\mathbf{y} = \mathbf{F}_u \mathbf{x} + \mathbf{e} \quad (1)$$

where $\mathbf{y} \in \mathbb{C}^{N_x N_y N_t}$ is the undersampled measurements in k-space and the unsampled points are filled with zero. \mathbf{F}_u is an undersampled Fourier encoding matrix, and $\mathbf{e} \in \mathbb{C}^{N_x N_y N_t}$ is acquisition noise. We want to reconstructed \mathbf{x} by solving the inverse problem of Eq. 1. However, the inverse problem is ill-posed, resulting in the reconstruction is not unique. In order to reconstruct \mathbf{x} , we constrain this inverse problem by adding some prior knowledge and solve the following optimization problem:

$$\min_{\mathbf{x}} \frac{1}{2} \|\mathbf{F}_u \mathbf{x} - \mathbf{y}\|_2^2 + \lambda \mathcal{R}(\mathbf{x}) \quad (2)$$

The first term is the data fidelity term, which ensures that the undersampled k-space of reconstruction is consistent with the actual undersampled measurements in k-space. The second term is often referred to as the regularization term, which contains a priori knowledge of \mathbf{x} . In the methods of CS, $\mathcal{R}(\mathbf{x})$ is usually the sparse prior of \mathbf{x} in some transformation fields, e.g. finite difference, wavelet transform and discrete cosine transformation.

In the methods of CNN, $\mathcal{R}(\mathbf{x})$ is the CNN prior of \mathbf{x} , which force \mathbf{x} to match the output of the CNN networks:

$$\min_{\mathbf{x}} \frac{1}{2} \|\mathbf{F}_u \mathbf{x} - \mathbf{y}\|_2^2 + \lambda \|\mathbf{x} - f_{CNN}(\mathbf{x}_u | \theta)\|_2^2 \quad (3)$$

Where \mathbf{x}_u is the undersampled image of \mathbf{x} and $f_{CNN}(\mathbf{x}_u | \theta)$ is the output of the CNN networks under the parameter θ , which is the result of the CNN networks reconstruction. The training process of the networks is to find the optimal parameter θ . Once the network is trained, the networks output is the reconstruction what we want. Since the training process is offline and Eq. 3 is equivalent to the online testing process, so CNN reconstruction is very time-saving.

B. The Proposed Method

1) *3D Complex Convolution*: MR data are usually complex-valued, but current deep learning is based on real-valued operations. The vast majority of the practice in CNN-MRI is to divide the complex-valued data into two channels, which consist of the real part and imaginary part. However, recent work on recurrent neural networks and older fundamental theoretical analysis suggests that complex numbers could have a richer representational capacity and could also facilitate noise-robust memory retrieval mechanisms [23]. Therefore, in this work will use complex convolution to replace the ordinary convolution.

Let $\mathbf{x} = \mathbf{x}_r + i\mathbf{x}_i$ is a 3D complex feature map and $\mathbf{W} = \mathbf{W}_r + i\mathbf{W}_i$ is a 3D complex filter matrix, where \mathbf{x}_r and \mathbf{x}_i , \mathbf{W}_r and \mathbf{W}_i are the real and imaginary parts respectively. Then, convolving the vector \mathbf{x} by the filter \mathbf{W} we obtain:

$$\mathbf{W} * \mathbf{x} = (\mathbf{W}_r * \mathbf{x}_r - \mathbf{W}_i * \mathbf{x}_i) + i(\mathbf{W}_r * \mathbf{x}_i + \mathbf{W}_i * \mathbf{x}_r) \quad (4)$$

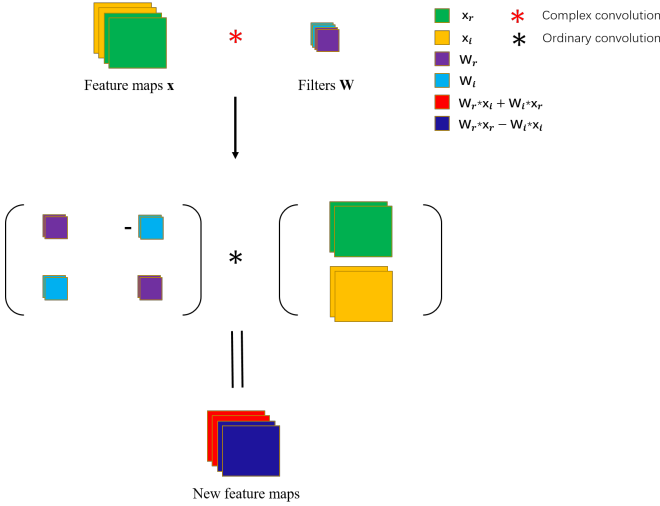


Fig. 1. An illustration of the complex convolution operator.

The matrix form of Eq. 4 is shown below:

$$\begin{bmatrix} R(\mathbf{W} * \mathbf{x}) \\ I(\mathbf{W} * \mathbf{x}) \end{bmatrix} = \begin{bmatrix} \mathbf{W}_r & -\mathbf{W}_i \\ \mathbf{W}_i & \mathbf{W}_r \end{bmatrix} * \begin{bmatrix} \mathbf{x}_r \\ \mathbf{x}_i \end{bmatrix} \quad (5)$$

The illustration of the complex convolution operator is shown in Fig. 1. It should be noted that the complex data are still circulated in a two-channels format, with the first half storing the real part and the second half storing the imaginary part. Once the complex convolution is required, the real and imaginary part are taken out and convolved according to Eq. 5.

2) *The Proposed DIMENSION Network:* In [21], a DC-CNN model has been proposed to reconstruct undersampled cardiac MR image. Despite the state-of-the-art reconstruction quality has been achieved using the D5C5 model, the frequency domain information hasn't been taken into consideration through pure image domain learning. In this work, we propose a novel convolutional neural network termed as DIMENSION for cardiac MR images reconstruction shown in Figure 2. DIMENSION network consists of two parts: the first part is frequency domain network for k-space completion termed as FDN, and we take five convolution layers as FDN; the second part is spatial domain network term as SDN, which is used to extract high-level features of images, and we take the D5C4 model of Jo et al [21] as SDN. The two are connected by Fourier inversion (see Inverse Fast Fourier Transform (IFFT) in Figure 2). What we need to explain here is that we chose D5C4 instead of D5C5 in order to make a fair comparison between DIMENSION and D5C5, both of which have 25 convolution layers in total. Or it can be understood as follows: we transform the D5C5 model into DIMENSION by changing a block of the D5C5 into FDN in order to take advantage of the frequency domain information. Specifically, the FDN consists of five 3D complex convolution layers and a k-space data consistency (KDC) layer. The details of FDN are shown in Table I. The role of the KDC layer is to correct MR images by the accurate k-space samples. Its noticeable that for the KDC layer of FDN, we don't need transform the output of

the fifth convolutional layer into frequency domain, because the output is already a completeness of k-space. Subsequent operations are the same as DC in [21]. The SDN consists of four blocks, each of which has five convolution layers. In addition to five convolution layers, each block also contains a residual connection and an image data consistency (IDC) layer [21]. The residual connection, which sums the output of each block with its input, allows the gradient to be directly back-propagated to earlier layers. The details of SDN are shown in Table II.

In fact, it's not the first time that both frequency domain and image domain information are learned simultaneously. Eo et al [17] proposed cross-domain convolutional neural networks (CNNs) for reconstructing undersampled MR images termed as KIKI-Net. They demonstrate that the combination of K-Net and I-Net is superior to single-domain CNNs. However, the training in [17] is performed with an incremental manner rather than an end-to-end manner in order to learn a KIKI-Net of which layer depth is more than 100 with small datasets. The incremental manner is extremely tedious and easy to appear overfitting because subsequent KI blocks can easily learn the noise in the datasets. Furthermore, KDC layer is not used in KIKI-Net, which is very helpful to the completion of k-space. At the same time, KIKI-Net is applied to 2D brain MR reconstruction while our DIMENSION network is applied to 3D cardiac MR reconstruction. In short, our DIMENSION model trains relatively shallow neural networks with an end-to-end manner for 3D cardiac MR reconstruction.

3) *The Proposed Multi-Supervised Loss:* In addition to introducing frequency domain and image domain learning in terms of network architecture, we also made important improvements in loss function. Our multi-supervised loss function is composed of primary loss and progressive loss shown in Fig. 3. The primary loss is the mean squared error (MSE) between the reconstructions and corresponding fully sampled images. The progressive loss is auxiliary loss include k-space loss and spatial loss. Let $\mathbf{k}_u, \mathbf{k}_c, \mathbf{k}_f, \mathbf{x}$ be the undersampled k-space, completed k-space, fully sampled k-space and fully sampled image respectively. Let $\mathbf{b}_1, \mathbf{b}_2, \mathbf{b}_3, \mathbf{b}_4$ be the output of block I1, block I2, block I3 and block I4 respectively. The k-space loss can be expressed as the formula:

$$\text{k-space loss} = \lambda_k \|\mathbf{k}_f - \mathbf{k}_c\|_2^2 \quad (6)$$

And the spatial loss is the weighted combination of Loss1, Loss2 and Loss3:

$$\text{spatial loss} = \sum_{i=1}^3 \lambda_i \|\mathbf{x} - \mathbf{b}_i\|_2^2 \quad (7)$$

where λ_k and $\lambda_i, i = 1, 2, 3$ are the respective weights of each loss. As mentioned above, the primary loss is MSE between the reconstructions (\mathbf{b}_4) and corresponding fully sampled images \mathbf{x} :

$$\text{primary loss} = \|\mathbf{x} - \mathbf{b}_4\|_2^2 \quad (8)$$

Finally, the total loss consists of these three loss:

$$\text{total loss} = \|\mathbf{x} - \mathbf{b}_4\|_2^2 + \sum_{i=1}^3 \lambda_i \|\mathbf{x} - \mathbf{b}_i\|_2^2 + \lambda_k \|\mathbf{k}_f - \mathbf{k}_c\|_2^2 \quad (9)$$

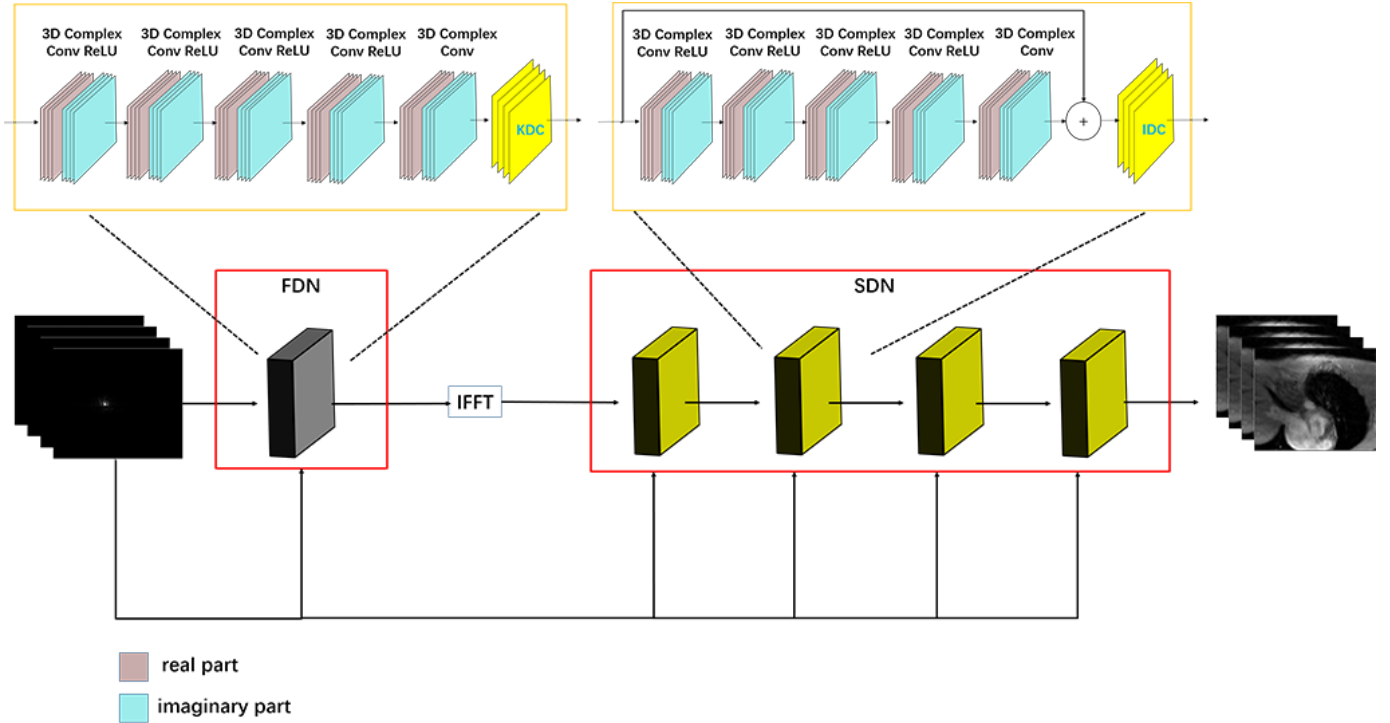


Fig. 2. The proposed DIMENSION network architecture for cardiac MR reconstruction.

TABLE I
THE PARAMETERS SETTING OF EACH BLOCK IN THE FDN.

Layer of K5	Input size	Number of filter	Filter size	Stride	Activation	Output
Complex conv1	117*120*6*2	64	3*3*3	[1, 1, 1]	ReLU	117*120*6*64
Complex conv2	117*120*6*64	64	3*3*3	[1, 1, 1]	ReLU	117*120*6*64
Complex conv3	117*120*6*64	64	3*3*3	[1, 1, 1]	ReLU	117*120*6*64
Complex conv4	117*120*6*64	64	3*3*3	[1, 1, 1]	ReLU	117*120*6*64
Complex conv5	117*120*6*64	2	3*3*3	[1, 1, 1]	None	117*120*6*2
Kspace data consistency	117*120*6*2	/	/	/	/	117*120*6*2

TABLE II
THE PARAMETERS SETTING OF EACH BLOCK IN THE SDN.

Layer of D5C4	Input size	Number of filter	Filter size	Stride	Activation	Output
Complex conv1	117*120*6*2	64	3*3*3	[1, 1, 1]	ReLU	117*120*6*64
Complex conv2	117*120*6*64	64	3*3*3	[1, 1, 1]	ReLU	117*120*6*64
Complex conv3	117*120*6*64	64	3*3*3	[1, 1, 1]	ReLU	117*120*6*64
Complex conv4	117*120*6*64	64	3*3*3	[1, 1, 1]	ReLU	117*120*6*64
Complex conv5	117*120*6*64	2	3*3*3	[1, 1, 1]	None	117*120*6*2
Residual	117*120*6*2	/	/	/	/	117*120*6*2
Kspace data consistency	117*120*6*2	/	/	/	/	117*120*6*2

The weights in Eq. 9 will be discussed in experimental section. Next, we will analyze the purpose of introducing k-space loss and spatial loss.

The set consisting of indices of sampled in k-space is defined as Ω . Then k-space sampling points can be divided into two parts: if point i has already been sampled, i is a member of set Ω , otherwise $i \notin \Omega$. The purpose of FDN is

to complete k-space and the quality of completion directly affects the image domain feature extraction of SDN and the final reconstruction. Therefore, it is necessary to force the completed k-space to approach the fully sampled k-space. If $i \in \Omega$, KDC layer (as shown in Fig. 2) is good at ensuring that the completed k-space is consistent with the actual sampled k-space. If $i \notin \Omega$, the k-space loss can make the completed

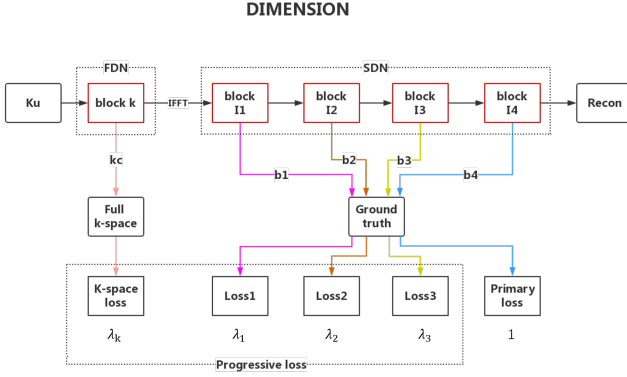


Fig. 3. The multi-supervised loss in DIMENSION networks.

k-space as close as possible to the fully sample k-space. The combination of KDC and k-space loss can guarantee the quality of completed k-space \mathbf{k}_c . The output of each block in SDN can be seen as reconstruction of different levels. Then the final output of the entire network can be seen as the final level of reconstruction. However, previous studies only made constraints on the final level reconstruction and used them as the loss function of the entire networks. This approach did not take full advantage of reconstruction information at other levels. Here, we put forward the spatial loss, which can constrain the reconstruction of different levels, making the reconstruction of each level closer to ground truth. As can be seen in Eq. 9, reconstruction in each level contributes to the final result, where the contributions are determined by individual weights.

III. EXPERIMENTAL RESULTS AND DISCUSSION

A. Setup

1) *Data acquisition*: We collected 101 fully sampled cardiac MR data from 12 subjects using 3T scanner (SIMENS MAGNETOM Trio) with T1-weighted flash sequence. Each scan contains a single slice FLASH acquisition with 25 temporal frames. The following parameters were used for FLASH scans: FOV 330×330 , acquisition matrix 192×192 , slice thickness 6mm, TR 3ms, TE 50ms and 24 coils. The raw multi-coil data of each frame was combined by adaptive coil combine method [24] to produce a single complex-valued image. There are three things to note in the process of data acquisition. Firstly, in order to obtain fully sampled images with high signal-to-noise ratio (SNR), the parallel acquisition technology (PAT) and all the filters are off during the whole scan. Secondly, FOV and acquisition matrix would make minor adjustments according to the physique of different subjects to ensure a good coverage of the heart in the image space. Thirdly, (breath hold). We randomly selected 90% of the entire dataset for training and 10% for testing. Deep learning has a high demand for data volume [25], but the collected data is far from the requirements of big data. Therefore, some data augmentation strategies have been applied. We shear the original image along the x, y and t direction. The sheared size is $117 \times 120 \times 6(x \times y \times t)$, and the stride along

the three directions is 7, 7 and 5 respectively. Finally, we obtained 17500 3D complex-valued cardiac MR data with the size of $117 \times 120 \times 6$. In this paper, we focus our attention on 1D random undersampling patterns. The original k-spaces were retrospectively undersampled by 4 times with 6 ACS. Specifically, we fully samples frequency-encodes (along k_x) and randomly undersamples the phase encodes (along k_y) according to a zero-mean Gaussian variable density function [7]. In subsequent sections, we will also discuss whether the proposed method can apply to other sampling patterns.

2) *Network training*: The network architecture and the parameters setting are given above. Here, our network framework is based on 3D complex convolutional layers rather than the ordinary convolutional layers. Since the datasets are complex-valued, we divide each data into two channels, where the channels store real and imaginary parts of the data. So the input of the network are 3D undersampled k-spaces $\mathbb{R}^{2N_x N_y N_t}$ and the output are 3D reconstructed images $\mathbb{R}^{2N_x N_y N_t}$. He initialization [26] was used to initialize the network weights. Rectifier Linear Units (ReLU) was selected as the nonlinear activation function. The mini-batch size was 20. The exponential decay learning rate [27] was used in all experiments and the initial learning rate was set to 0.0001 with decay 0.95. All the models were trained by the Adam optimizer [28] with parameters $\beta_1 = 0.9, \beta_2 = 0.999$ and $\epsilon = 10^{-8}$. The models were implemented on an Ubuntu 16.04 LTS (64-bit) operating system equipped with an Intel Xeon E5-2640 Central Processing Unit (CPU) and Tesla TITAN Xp Graphics Processing Unit (GPU, 12GB memory) in the open framework Tensorflow [29] with CUDA and CUDNN support.

3) *Performance evaluation*: For a quantitative evaluation, mean square error (MSE), peak signal to noise ratio (PSNR) and structural similarity index (SSIM) [30] were measured as follows:

$$\text{MSE} = \frac{\|Ref - Rec\|_2^2}{\|Ref\|_2^2} \quad (10)$$

$$\text{PSNR} = 20 \log_{10} \frac{\max(Ref) \sqrt{N}}{\|Ref - Rec\|_2} \quad (11)$$

$$\text{SSIM} = l(Ref, Rec) \cdot c(Ref, Rec) \cdot s(Ref, Rec) \quad (12)$$

Where Rec is the reconstructed image, Ref denotes the reference image and N is the total number of image pixels. The SSIM index is a multiplicative combination of the luminance term, the contrast term, and the structural term (details shown in [30]).

B. Does DIMENSION Model Work?

To demonstrate the efficacy of DIMENSION, which combines k-space domain learning and image domain learning, we compare it with the state-of-the-art method D5C5. The two networks have the same amount of network parameters. And for fair comparison, the networks hyperparameters are also set to the same. The reconstructions of D5C5 and DIMENSION are shown in Fig. 4. The display ranges for the error maps is [00.07]. For 4-fold acceleration, one can see that DIMENSION model outperforms D5C5 model in terms of artifacts removing and details reservation (see the arrows in Fig. 4 (e) and

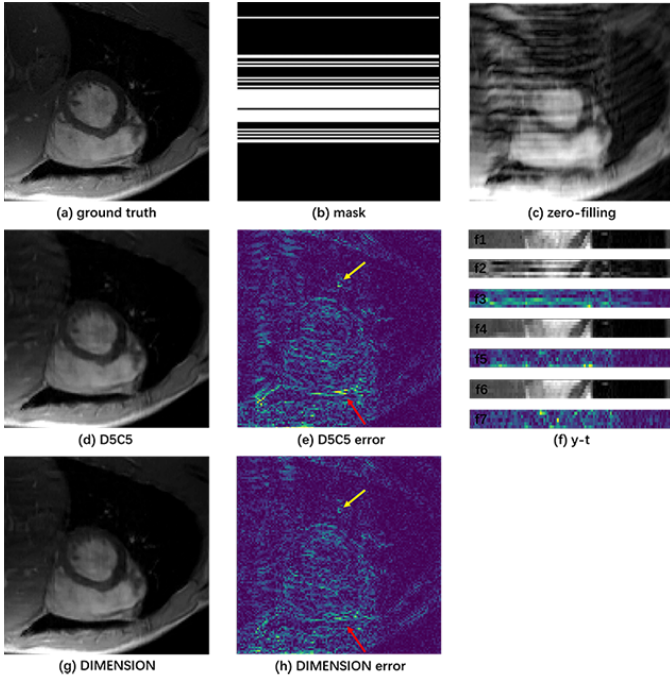


Fig. 4. The reconstructions of D5C5 and DIMENSION. (a) ground truth, (b) mask, (c) zero-filling image, (d) D5C5 reconstruction, (g) DIMENSION reconstruction, (e) and (h) their corresponding error maps with display ranges $[0, 0.07]$. (f) Extractions of 55th slice along y and temporal dimensions ($y-t$), from top (f1) to bottom (f7): (f1) ground truth, (f2) zero-filling image, (f3) error map of zero-filling, (f4) D5C5 reconstruction, (f5) error map of D5C5, (f6) DIMENSION reconstruction, (f7) error map of DIMENSION.

TABLE III
THE MSE, PSNR AND SSIM OF ZERO-FILLING, D5C5 AND DIMENSION.

Models	MSE	PSNR	SSIM
Zero-filling	0.004724	23.2146	0.7637
D5C5	0.000301	35.1694	0.9775
DIMENSION	0.000176	37.5857	0.9846

The bolder ones mean better.

(h)). To explore the reconstructed results in the direction of temporal, we show the slices along y and temporal dimensions ($y-t$). From the $y-t$ images (Fig. 4 (f)), we can see that the reconstruction of DIMENSION has a smaller error map, which is consistent with the above conclusion along the temporal dimension. We also show the quantitative evaluations of DIMENSION and D5C5 on the test MRI datasets in Table III.

From the three performance indicators of MSE, PSNR and SSIM, it can be seen that DIMENSION has been significantly improved over D5C5 (0.000128 in MSE, 2.4163dB in PSNR and 0.071 in SSIM). Thus it can be seen that DIMENSION is superior to D5C5 in both visual results and quantitative indicators.

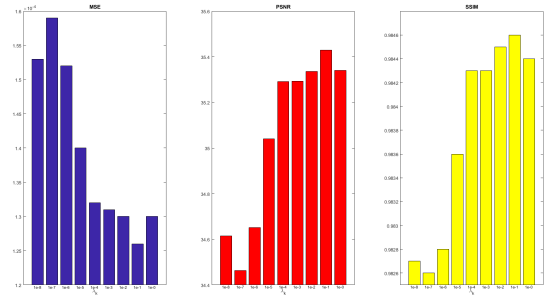


Fig. 5. The histograms of the average MSE, PSNR, SSIM on the test set with different λ_k . Here, λ_k goes from 10^{-8} to 10^{-1}

In conclusion, DIMENSION can effectively learning cross-domain information and improve MR reconstruction by using both image domain and frequency domain information. The respective roles of image domain network and frequency domain network can be found in [18]. Subsequent models are all constructed based on the DIMENSION model.

C. Does K-space Loss Work?

This section mainly explores whether k-space loss can improve the reconstruction. The purpose of introducing k-space loss is to further constrain FDN to get a better completed k-space. The k-space loss is shown in Eq. 6. We select the MSE between completed k-space and fully sampled k-space as our k-space loss and the total loss function of this section is shown below:

$$\text{total loss1} = \|\mathbf{x} - \mathbf{b}_4\|_2^2 + \lambda_k \|\mathbf{k}_f - \mathbf{k}_c\|_2^2 \quad (13)$$

where λ_k is a hyperparameter, whose selection has a great influence on the reconstruction [25]. If the choice of λ_k is not appropriate, it is likely to worsen the reconstruction. In order to find appropriate λ_k , we trained a series of DIMENSION with different λ_k and then tested them on the same test set. The average MSE, PSNR, SSIM on the test set are shown in Fig. 5. We can observe that when $\lambda_k = 10^{-1}$, DIMENSION gets the lowest MSE, the highest PSNR and the highest SSIM. So we pick 10^{-1} as the most appropriate value for λ_k .

After choosing the appropriate λ_k , we can explore whether k-space loss is helpful for reconstruction. We refer to the DIMENSION model that introduces k-space loss as DIMENSION-KLoss. The comparison results of DIMENSION and DIMENSION-KLoss are shown in Fig. 6. Obviously, DIMENSION -KLoss gets better reconstruction, especially in removing artifacts. We can get the same results from the $y-t$ images (Fig. 6 (f)). The quantitative measurements can be found in Table IV. K-space loss can significantly improve the MSE, PSNR and SSIM (0.000044 in MSE, 2.3390dB in PSNR and 0.0029 in SSIM). Therefore, we can conclude without prejudice that k-space loss can effectively improve the cardiac MR reconstruction. With the joint action of KDC and k-space loss, satisfactory completed k-space can be obtained.

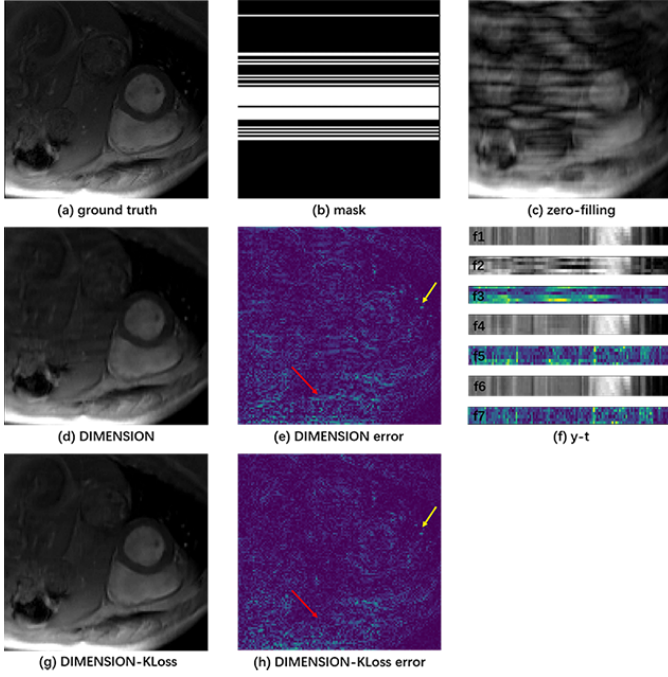


Fig. 6. The reconstructions of DIMENSION and DIMENSION-KLoss. (a) ground truth, (b) mask, (c) zero-filling image, (d) DIMENSION reconstruction, (g) DIMENSION-KLoss reconstruction, (e) and (h) their corresponding error maps with display ranges $[0, 0.07]$. (f) Extractions of 55^{th} slice along y and temporal dimensions ($y-t$), from top (f1) to bottom (f7): (f1) ground truth, (f2) zero-filling image, (f3) error map of zero-filling, (f4) DIMENSION reconstruction, (f5) error map of DIMENSION, (f6) DIMENSION-KLoss reconstruction, (f7) error map of DIMENSION-KLoss.

TABLE IV
THE MSE, PSNR AND SSIM OF ZERO-FILLING, DIMENSION AND DIMENSION-KLOSS.

Models	MSE	PSNR	SSIM
Zero-filling	0.004881	22.7804	0.8016
DIMENSION	0.000105	39.4711	0.9910
DIMENSION-KLoss	0.000061	41.8101	0.9939

The bolder ones mean better.

D. Does Spatial Loss Work?

In this section, we demonstrate whether spatial loss can improve MR reconstruction. The so-called spatial loss (in Eq. 7) is to constrain the reconstructions of different blocks with individual weights. We can regard the outputs of the blocks in the shallow layers as the preliminary reconstructions, and the output of the block in the last layer as the final reconstruction. The relationship between the preliminary reconstruction and the final reconstruction is progressive. To demonstrate the effectiveness of spatial loss, we use the combination of the primary loss and the spatial loss as the total loss in this section

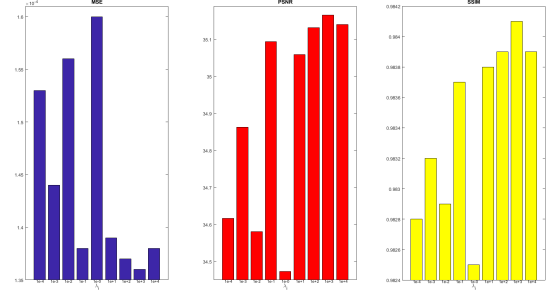


Fig. 7. The histograms of the average MSE, PSNR, SSIM on the test set with different $\lambda_i, i = 1, 2, 3$. Here, $\lambda_1 = \lambda_2 = \lambda_3$ and equal to $10^{-4}, 10^{-3}, \dots, 10^3, 10^4$

TABLE V
THE MSE, PSNR AND SSIM OF ZERO-FILLING, DIMENSION AND DIMENSION-SLOSS1.

Models	MSE	PSNR	SSIM
Zero-filling	0.004211	23.7471	0.8208
DIMENSION	0.000261	35.8304	0.9738
DIMENSION-SLoss1	0.000214	36.6892	0.9764

The bolder ones mean better.

of the experiment:

$$\text{total loss2} = \|\mathbf{x} - \mathbf{b}_d\|_2^2 + \sum_{i=1}^3 \lambda_i \|\mathbf{x} - \mathbf{b}_i\|_2^2 \quad (14)$$

As with λ_k , the choice of $\lambda_i, i = 1, 2, 3$ have a significant impact on reconstruction. There are two ways to select λ_i : the first is to take the same values for these three weights, and the second is to take increasing or decreasing values for these three weights. First, lets consider the case when each λ_i takes the same value. We trained a series of DIMENSION models, where $\lambda_i, i = 1, 2, 3$, in turn, equal to $10^{-4}, 10^{-3}, \dots, 10^3, 10^4$. Then all these models are tested on the same test set. The quantitative results are shown in Fig. 7. We can see that $\lambda_1 = \lambda_2 = \lambda_3 = 10^3$ has the best performance on the test set with the lowest MSE, the highest PSNR and the highest SSIM. We refer to the DIMENSION model of $\lambda_1 = \lambda_2 = \lambda_3 = 10^3$ as DIMENSION-SLoss1. Fig. 8 shows the experimental results of DIMENSION and DIMENSION-SLoss1. We can clearly see that DIMENSION-SLoss1 has fewer artifacts and retains details better from the error maps (as shown by the red and yellow arrows in Fig. 8 (e, h, f5, f7)). The quantitative measurements can be found in Table V, from which we can conclude that spatial loss with the same weights can effectively improve the MSE, PSNR and SSIM (0.000047 in MSE, 0.8588dB in PSNR and 0.0026 in SSIM).

Secondly, lets consider the case when these three weights take increasing or decreasing values. The values of $\lambda_i, i =$

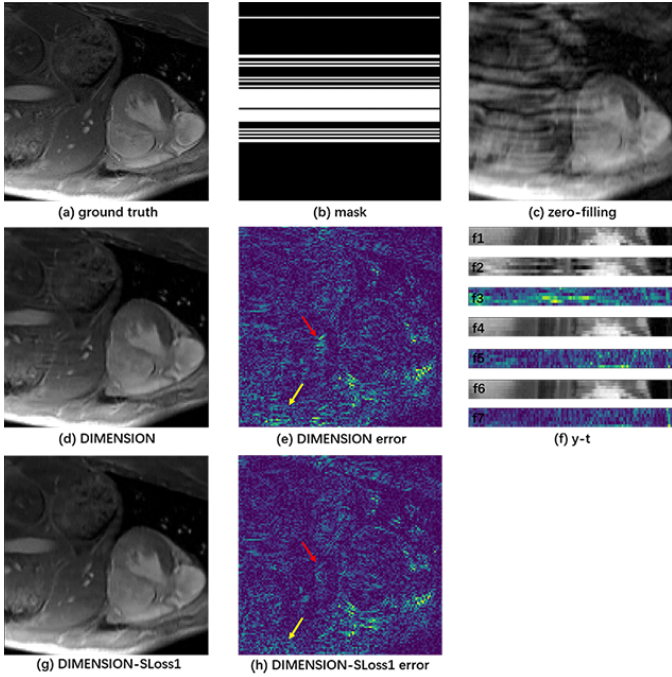


Fig. 8. The reconstructions of DIMENSION and DIMENSION-SLoss1. (a) ground truth, (b) mask, (c) zero-filling image, (d) DIMENSION reconstruction, (g) DIMENSION-SLoss1 reconstruction, (e) and (h) their corresponding error maps with display ranges [0, 0.07]. (f) Extractions of 55th slice along y and temporal dimensions (y-t), from top (f1) to bottom (f7): (f1) ground truth, (f2) zero-filling image, (f3) error map of zero-filling, (f4) DIMENSION reconstruction, (f5) error map of DIMENSION, (f6) DIMENSION-SLoss1 reconstruction, (f7) error map of DIMENSION-SLoss1.

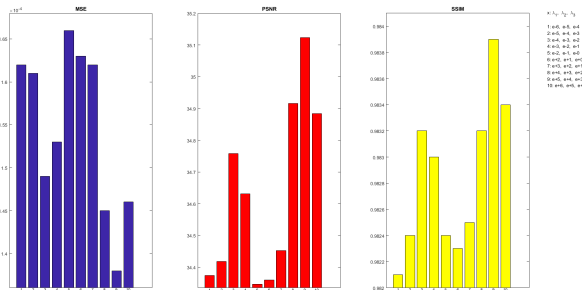


Fig. 9. The histograms of the average MSE, PSNR, SSIM on the test set with different $\lambda_i, i = 1, 2, 3$, which are shown in Table VI.

1, 2, 3 are shown in Table VI. We have considered a total of 10 cases, where $\lambda_i, i = 1, 2, 3$ are increasing in the first five and decreasing in the last five. The quantitative results are shown in Fig. 9. Obviously, we find that the ninth case gets the best quantization results, where the MSE is lowest, the PSNR and SSIM are highest. So, we chose $\lambda_1 = 10^5, \lambda_2 = 10^4, \lambda_3 = 10^3$ as our preferred weights. We refer to the DIMENSION model of $\lambda_1 = 10^5, \lambda_2 = 10^4, \lambda_3 = 10^3$ as DIMENSION-SLoss2 and the reconstructions of DIMENSION and DIMENSION-SLoss2 are shown in Fig. 10. We can clearly see that DIMENSION-SLoss2 has fewer artifacts and retains details better from the error maps (as shown by the red and yellow arrows in Fig. 10 (e, h, f5, f7)). The quantitative measurements can be found

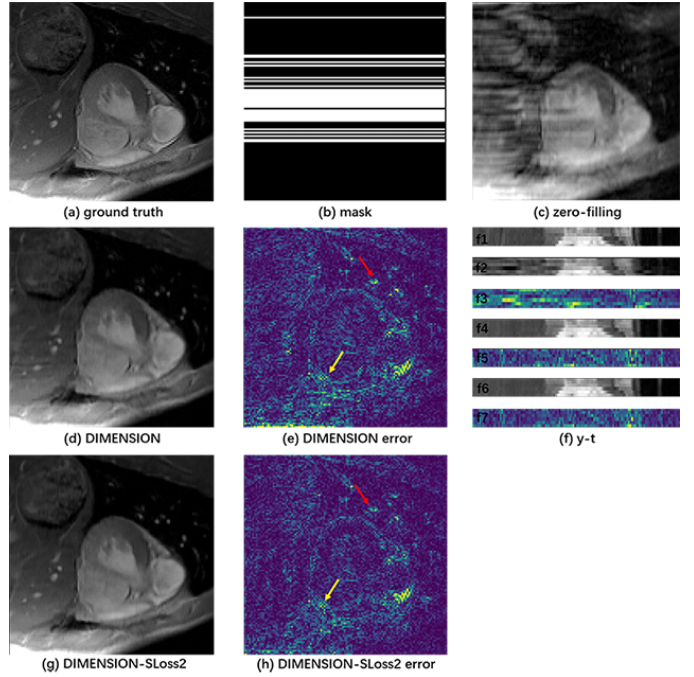


Fig. 10. The reconstructions of DIMENSION and DIMENSION-SLoss2. (a) ground truth, (b) mask, (c) zero-filling image, (d) DIMENSION reconstruction, (g) DIMENSION-SLoss2 reconstruction, (e) and (h) their corresponding error maps with display ranges [0, 0.07]. (f) Extractions of 55th slice along y and temporal dimensions (y-t), from top (f1) to bottom (f7): (f1) ground truth, (f2) zero-filling image, (f3) error map of zero-filling, (f4) DIMENSION reconstruction, (f5) error map of DIMENSION, (f6) DIMENSION-SLoss2 reconstruction, (f7) error map of DIMENSION-SLoss2.

in Table VII, from which we can conclude that spatial loss with the decreasing weights can effectively improve the MSE, PSNR and SSIM (0.000066 in MSE, 1.1460dB in PSNR and 0.0042 in SSIM).

Then, it's natural to think about which of these two ways to select λ_i works better. The quantitative results and reconstructions of DIMENSION-SLoss1 and DIMENSION-SLoss2 are respectively shown in Fig. 11 and Table VIII.

The two models have similar reconstructed results, but the quantization results of DIMENSION-SLoss1 are slightly improved, so we choose DIMENSION-SLoss1 as our final reconstructed model. To sum up, the total loss that we finally selected is shown in the following formula:

$$\text{total loss} = \|\mathbf{x} - \mathbf{b}_4\|_2^2 + \sum_{i=1}^3 10^3 \|\mathbf{x} - \mathbf{b}_i\|_2^2 + 10^{-1} \|\mathbf{k}_f - \mathbf{k}_c\|_2^2 \quad (15)$$

E. Comparison to The State-of-the-art Methods

Based on the above sections, the network we used is DIMENSION (as shown in Fig. 2) and the multi-supervised loss we selected is shown Eq. 15. In this section, we will demonstrate the effectiveness of the proposed method by comparing this method with the traditional CS (k-t FOCUSS [7], k-t SLR [8], S+L [9]) methods and the state-of-the-art CNN method (D5C5 [21]). All CS-based methods select their single-channel versions. For fair comparison, we adjust the parameters of the CS-MRI methods to their best performance.

TABLE VI
TEN CASES OF $\lambda_i, i = 1, 2, 3$ TAKING DIFFERENT VALUES.

λ_i	Case 1	Case 2	Case 3	Case 4	Case 5	Case 6	Case 7	Case 8	Case 9	Case 10
λ_1	10^{-6}	10^{-5}	10^{-4}	10^{-3}	10^{-2}	10^2	10^3	10^4	10^5	10^6
λ_2	10^{-5}	10^{-4}	10^{-3}	10^{-2}	10^{-1}	10^1	10^2	10^3	10^4	10^5
λ_3	10^{-4}	10^{-3}	10^{-2}	10^{-1}	10^{-0}	10^0	10^1	10^2	10^3	10^4

TABLE VII
THE MSE, PSNR AND SSIM OF ZERO-FILLING, DIMENSION AND DIMENSION-SLoss2.

Models	MSE	PSNR	SSIM
Zero-filling	0.003578	24.0981	0.8242
DIMENSION	0.000285	35.0817	0.9701
DIMENSION-SLoss2	0.000219	36.2277	0.9743

The bolder ones mean better.

TABLE VIII
THE MSE, PSNR AND SSIM OF ZERO-FILLING, DIMENSION-SLoss1 AND DIMENSION-SLoss2.

Models	MSE	PSNR	SSIM
Zero-filling	0.004297	23.6684	0.8169
DIMENSION-SLoss1	0.000083	40.8160	0.9918
DIMENSION-SLoss2	0.000094	40.2876	0.9913

The bolder ones mean better.

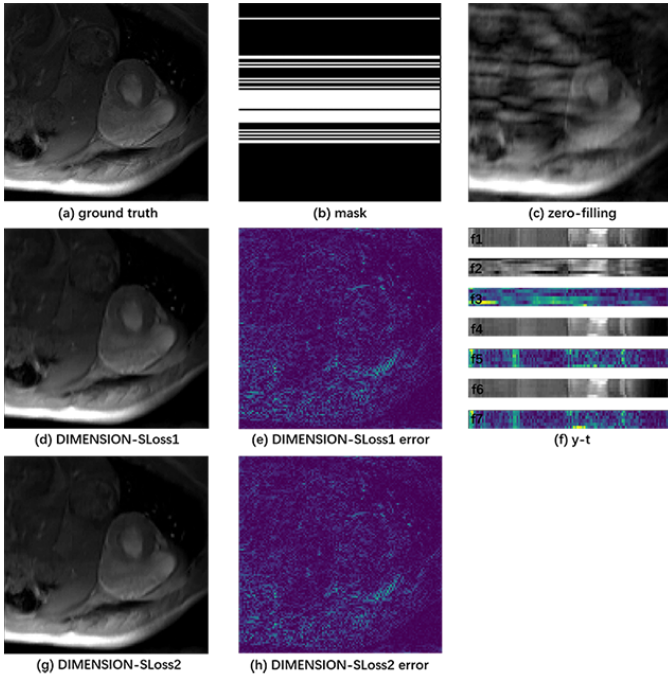


Fig. 11. The reconstructions of DIMENSION-SLoss1 and DIMENSION-SLoss2. (a) ground truth, (b) mask, (c) zero-filling image, (d) DIMENSION-SLoss1 reconstruction, (g) DIMENSION-SLoss2 reconstruction, (e) and (h) their corresponding error maps with display ranges [0, 0.07]. (f) Extractions of 55th slice along y and temporal dimensions (y-t), from top (f1) to bottom (f7): (f1) ground truth, (f2) zero-filling image, (f3) error map of zero-filling, (f4) DIMENSION-SLoss1 reconstruction, (f5) error map of DIMENSION-SLoss1, (f6) DIMENSION-SLoss2 reconstruction, (f7) error map of DIMENSION-SLoss2.

The visualization of reconstructions from different methods are shown in Fig. 12. The k-t SLR removes artifacts better than the k-t FOCUSS and S+L. However, these three CS-based

TABLE IX
THE MSE, PSNR, SSIM AND RUNNING TIME OF ZERO-FILLING, K-T FOCUSS, K-T SLR, D5C5 AND THE PROPOSED METHOD.

Models	MSE	PSNR	SSIM
Zero-filling	0.006003	22.2162	0.5346
k-t FOCUSS	0.000308	35.1201	0.9162
k-t SLR	0.000157	38.0534	0.9532
S+L	0.000333	34.7778	0.9616
D5C5	0.000121	39.1788	0.9548
DIMENSION	0.000086	40.6256	0.9655

The bolder ones mean better.

methods lose more structural details than the CNN-based methods. Compared with the D5C5 method, the proposed method can not only retain the details, but also remove the artifacts better.

We show the evaluation indexes in Table IX. Note that the CNN-based methods outperform the CS-based methods in all three performance indexes. We observe the proposed DIMENSION model with additional loss achieves the optimal performance in MSE, PSNR and SSIM indexer among the compared methods. The reconstruction time of different methods is shown in Table X. All the methods run on the same CPU Intel Xeon E5-2640. It can be seen that the reconstruction

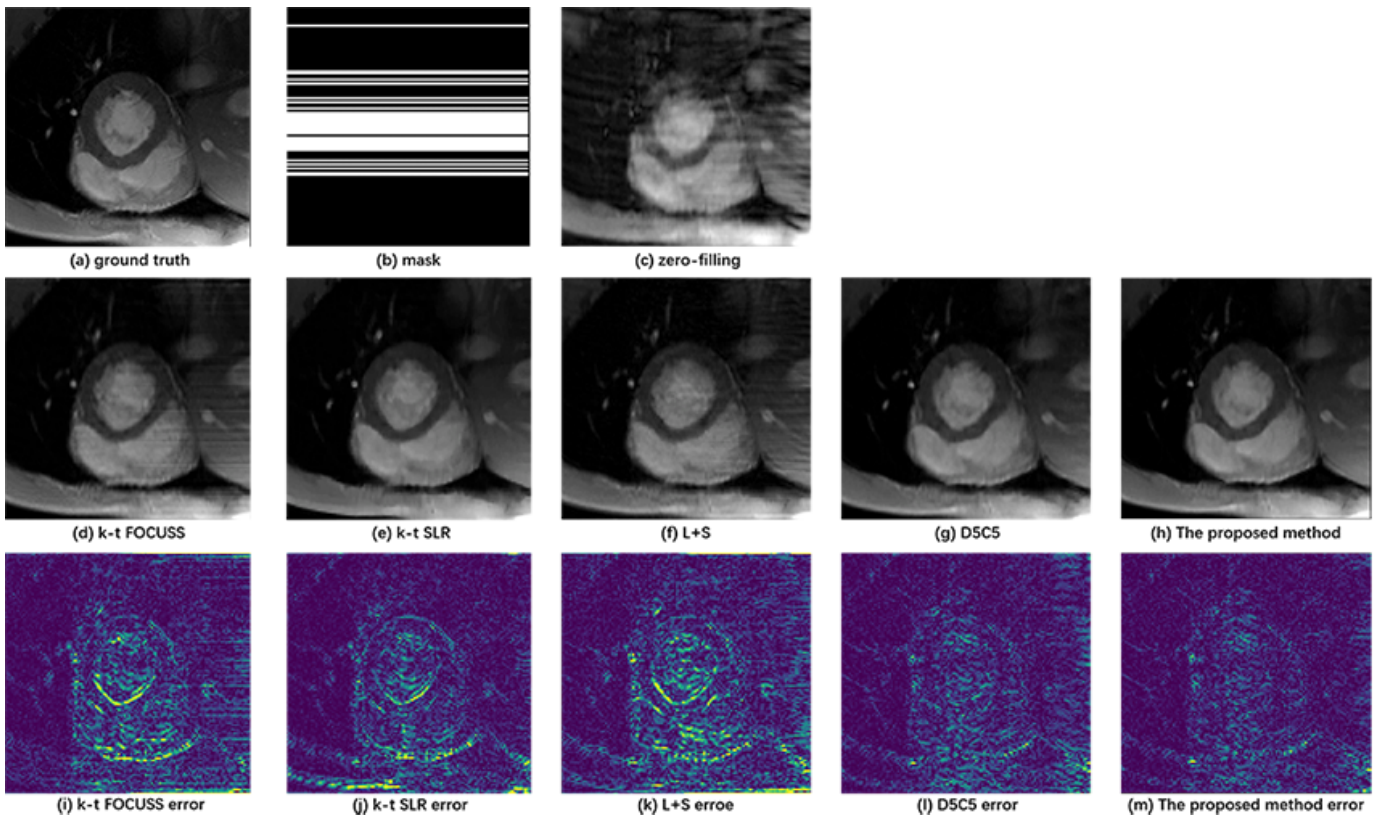


Fig. 12. The comparison of cardiac MR reconstructions from different methods (k-t FOCUSS, k-t SLR, L+S, D5C5, the proposed method). (a) ground truth, (b) mask, (c) zero-filling image, (d) k-t FOCUSS reconstruction, (e) k-t SLR reconstruction, (f) L+S reconstruction, (g) D5C5 reconstruction, (h) the proposed method reconstruction; (i), (j), (k), (l) and (m) their corresponding error maps with display ranges [0, 0.07].

TABLE X
THE RECONSTRUCTION TIME OF K-T SLR, L+S, D5C5, DIMENSION
METHODS.

Methods	k-t SLR	L+S	D5C5	DIMENSION
Running time/s	14.7249	17.3808	4.9318	4.8845

The bolder ones mean better.

time of the CNN-based methods is significantly shorter than the CS-based methods.

IV. CONCLUSION AND OUTLOOK

In this work, we propose a dynamic MR imaging method with both k-space and spatial prior knowledge integrated via multi-supervised network training, dubbed as DIMENSION. Our improvement is mainly reflected in the network structure and loss function. First, in the terms of network structure, we propose DIMENSION network, which can fully combine frequency domain and spatial domain prior information. This is the first time that cross-domain learning is applied to dynamic MR imaging. Second, we propose a novel multi-supervised loss function strategy. We introduce k-space loss, which can force the completed k-space from the frequency domain network to be as close as possible to full sampled k-space. At the same time, we also introduce spatial loss, which can constrain the reconstruction results of different levels of the spatial domain network. This loss function strategy avoids

the single-supervised training with only a single loss for the network and provides different levels of supervision for the entire network. We compared the proposed approach with k-t FOCUSS, k-t SLR and the state-of-the-art CNN-based method. Experimental results show that the proposed network structure and loss strategy can further improve dynamic MR reconstruction.

REFERENCES

- [1] W. Kaiser and E. Zeitler, "Mr imaging of the breast: fast imaging sequences with and without gd-dtpa. preliminary observations." *Radiology*, vol. 170, no. 3, pp. 681–686, 1989.
- [2] D. K. Sodickson and W. J. Manning, "Simultaneous acquisition of spatial harmonics (smash): fast imaging with radiofrequency coil arrays," *Magnetic resonance in medicine*, vol. 38, no. 4, pp. 591–603, 1997.
- [3] D. L. Donoho, "Compressed sensing," *IEEE Transactions on information theory*, vol. 52, no. 4, pp. 1289–1306, 2006.
- [4] E. J. Candès *et al.*, "Compressive sampling," in *Proceedings of the international congress of mathematicians*, vol. 3. Madrid, Spain, 2006, pp. 1433–1452.
- [5] M. Lustig, D. Donoho, and J. M. Pauly, "Sparse mri: The application of compressed sensing for rapid mr imaging," *Magnetic Resonance in Medicine: An Official Journal*

- of the *International Society for Magnetic Resonance in Medicine*, vol. 58, no. 6, pp. 1182–1195, 2007.
- [6] J. Tsao, P. Boesiger, and K. P. Pruessmann, “k-t blast and k-t sense: dynamic mri with high frame rate exploiting spatiotemporal correlations,” *Magnetic Resonance in Medicine: An Official Journal of the International Society for Magnetic Resonance in Medicine*, vol. 50, no. 5, pp. 1031–1042, 2003.
- [7] H. Jung, J. C. Ye, and E. Y. Kim, “Improved k–t blast and k–t sense using focuss,” *Physics in Medicine & Biology*, vol. 52, no. 11, p. 3201, 2007.
- [8] S. G. Lingala, Y. Hu, E. DiBella, and M. Jacob, “Accelerated dynamic mri exploiting sparsity and low-rank structure: kt slr,” *IEEE transactions on medical imaging*, vol. 30, no. 5, pp. 1042–1054, 2011.
- [9] R. Otazo, E. Candès, and D. K. Sodickson, “Low-rank plus sparse matrix decomposition for accelerated dynamic mri with separation of background and dynamic components,” *Magnetic Resonance in Medicine*, vol. 73, no. 3, pp. 1125–1136, 2015.
- [10] J. Caballero, A. N. Price, D. Rueckert, and J. V. Hajnal, “Dictionary learning and time sparsity for dynamic mr data reconstruction,” *IEEE transactions on medical imaging*, vol. 33, no. 4, pp. 979–994, 2014.
- [11] J. Sun, H. Li, Z. Xu *et al.*, “Deep admm-net for compressive sensing mri,” in *Advances in Neural Information Processing Systems*, 2016, pp. 10–18.
- [12] K. Hammernik, T. Klatzer, E. Kobler, M. P. Recht, D. K. Sodickson, T. Pock, and F. Knoll, “Learning a variational network for reconstruction of accelerated mri data,” *Magnetic resonance in medicine*, vol. 79, no. 6, pp. 3055–3071, 2018.
- [13] F. Knoll, K. Hammernik, E. Kobler, T. Pock, M. P. Recht, and D. K. Sodickson, “Assessment of the generalization of learned image reconstruction and the potential for transfer learning,” *Magnetic resonance in medicine*, 2018.
- [14] S. Wang, Z. Su, L. Ying, X. Peng, S. Zhu, F. Liang, D. Feng, and D. Liang, “Accelerating magnetic resonance imaging via deep learning,” in *Biomedical Imaging (ISBI), 2016 IEEE 13th International Symposium on*. IEEE, 2016, pp. 514–517.
- [15] K. Kwon, D. Kim, and H. Park, “A parallel mr imaging method using multilayer perceptron,” *Medical physics*, vol. 44, no. 12, pp. 6209–6224, 2017.
- [16] Y. Han, J. Yoo, H. H. Kim, H. J. Shin, K. Sung, and J. C. Ye, “Deep learning with domain adaptation for accelerated projection-reconstruction mr,” *Magnetic resonance in medicine*, vol. 80, no. 3, pp. 1189–1205, 2018.
- [17] B. Zhu, J. Z. Liu, S. F. Cauley, B. R. Rosen, and M. S. Rosen, “Image reconstruction by domain-transform manifold learning,” *Nature*, vol. 555, no. 7697, p. 487, 2018.
- [18] T. Eo, Y. Jun, T. Kim, J. Jang, H.-J. Lee, and D. Hwang, “Kiki-net: cross-domain convolutional neural networks for reconstructing undersampled magnetic resonance images,” *Magnetic resonance in medicine*, 2018.
- [19] L. Sun, Z. Fan, Y. Huang, X. Ding, and J. Paisley, “Compressed sensing mri using a recursive dilated network,” 2018.
- [20] T. M. Quan, T. Nguyen-Duc, and W.-K. Jeong, “Compressed sensing mri reconstruction using a generative adversarial network with a cyclic loss,” *IEEE transactions on medical imaging*, vol. 37, no. 6, pp. 1488–1497, 2018.
- [21] J. Schlemper, J. Caballero, J. V. Hajnal, A. N. Price, and D. Rueckert, “A deep cascade of convolutional neural networks for dynamic mr image reconstruction,” *IEEE transactions on Medical Imaging*, vol. 37, no. 2, pp. 491–503, 2018.
- [22] C. Qin, J. V. Hajnal, D. Rueckert, J. Schlemper, J. Caballero, and A. N. Price, “Convolutional recurrent neural networks for dynamic mr image reconstruction,” *IEEE transactions on medical imaging*, 2018.
- [23] C. Trabelsi, O. Bilaniuk, Y. Zhang, D. Serdyuk, S. Subramanian, J. F. Santos, S. Mehri, N. Rostamzadeh, Y. Bengio, and C. J. Pal, “Deep complex networks,” *arXiv preprint arXiv:1705.09792*, 2017.
- [24] D. O. Walsh, A. F. Gmitro, and M. W. Marcellin, “Adaptive reconstruction of phased array mr imagery,” *Magnetic Resonance in Medicine: An Official Journal of the International Society for Magnetic Resonance in Medicine*, vol. 43, no. 5, pp. 682–690, 2000.
- [25] Y. LeCun, Y. Bengio, and G. Hinton, “Deep learning,” *nature*, vol. 521, no. 7553, p. 436, 2015.
- [26] K. He, X. Zhang, S. Ren, and J. Sun, “Delving deep into rectifiers: Surpassing human-level performance on imagenet classification,” in *Proceedings of the IEEE international conference on computer vision*, 2015, pp. 1026–1034.
- [27] M. D. Zeiler, “Adadelta: an adaptive learning rate method,” *arXiv preprint arXiv:1212.5701*, 2012.
- [28] D. P. Kingma and J. Ba, “Adam: A method for stochastic optimization,” *arXiv preprint arXiv:1412.6980*, 2014.
- [29] M. Abadi, P. Barham, J. Chen, Z. Chen, A. Davis, J. Dean, M. Devin, S. Ghemawat, G. Irving, M. Isard *et al.*, “Tensorflow: a system for large-scale machine learning,” in *OSDI*, vol. 16, 2016, pp. 265–283.
- [30] Z. Wang, A. C. Bovik, H. R. Sheikh, and E. P. Simoncelli, “Image quality assessment: from error visibility to structural similarity,” *IEEE transactions on image processing*, vol. 13, no. 4, pp. 600–612, 2004.